Mechanisms of Spontaneous and Amplified Spontaneous Emission in $CH_3NH_3PbI_3$ Perovskite Thin Films Integrated in an Optical Waveguide

I. Suárez,[1,2,*] E.J. Juárez-Pérez,[3,4] V.S. Chirvony,[1] I. Mora-Seró,[5] and J.P. Martínez-Pastor[1,†]

[1] *UMDO, Instituto de Ciencia de los Materiales, Universidad de Valencia, 46071 Valencia, Spain*

[2] *Escuela Técnica Superior de Ingeniería, Universidad de Valencia, C/Avenida de la Universidad s/n, 46100 Burjassot, Valencia, Spain*

[3] *ARAID, Government of Aragon, 50018 Zaragoza, Spain*

[4] *Institute of Nanoscience of Aragon (INA), University of Zaragoza, 50018 Zaragoza, Spain*

[5] *Institute of Advanced Materials (INAM), Universitat Jaume I, 12071 Castelló, Spain*

(Received 24 November 2019; accepted 13 May 2020; published 30 June 2020)

In this paper, the physical mechanisms responsible for optical gain in $CH_3NH_3PbI_3$ (MAPI) polycrystalline thin films are investigated experimentally and theoretically. Waveguide structures composed by a MAPI film embedded in between PMMA and silica layers are used as an efficient geometry to confine emitted light in MAPI films and minimize the energy threshold for amplified spontaneous emission (ASE). We show that photogenerated exciton density at the ASE threshold is as low as $(2.4 - 12) \times 10^{16}\ \mathrm{cm}^{-3}$, which is below the Mott transition density reported for this material and the threshold transparency condition deduced with the free-carrier model. Such a low threshold indicates that the formation of excitons plays an important role in the generation of optical gain in MAPI films. The rate-equation model including gain is incorporated into a beam-propagation algorithm to describe waveguided spontaneous emission and ASE in MAPI films, while using the optical parameters experimentally determined in this work. This model is a useful tool to design active photonic devices based on MAPI and other metal-halide semiconductors.

DOI: 10.1103/PhysRevApplied.13.064071

I. INTRODUCTION

Metal-halide perovskites (MHP) have arisen as exceptional semiconductors for new generation optoelectronics. Although initially the interest in these materials was focused on photovoltaics [1–4], they have also demonstrated outstanding capabilities for integration of multiple functionalities in photonic devices [5,6]. In particular, with a high efficiency of absorption and emission, bandgap tunability, and a possibility to eliminate defects by passivation [7], MHPs have become a very promising optical-gain media [8]. Indeed, from the earliest publications with $CH_3NH_3PbI_3$ (MAPI) polycrystalline thin films [9] MHPs have exhibited exceptional optical-gain performances in the visible and near-infrared wavelength range [10]. Low thresholds (1–10 $\mathrm{nJ/cm}^2$) of stimulated emission under pulsed excitation were demonstrated in several publications by incorporating perovskite layers into waveguides [11,12], optical resonators [13–15], or by synthetizing this material as microdisks [16–18] and nanowires [19,20]. More recently, lasing operation in MAPI films under continuous-wave operation was demonstrated [21–23].

However, despite the high interest in the topic with a significant amount of works published in recent years, the underlying mechanisms of the amplified spontaneous-emission (ASE) process in MHP materials are not completely understood as compared to the case of other semiconductors, which is one of the main goals of this paper. There are several works devoted to the photophysics responsible for PL [24–26], the nonradiative losses in traps limiting the optical gain [9,27], or the role of excitons in PL generation [28]. However, it is still an open question about the physical mechanism of optical gain, a prerequisite for lasing. According to the semiconductor's theory [29], what species are dominant, free electrons and holes or excitons, would be determined by the exciton binding energy at a given temperature through Saha's equation, whereas the Mott density would represent the transition between the insulating exciton gas and the metallic electron-hole plasma [30]. Some publications argue that free carriers are responsible for ASE in MAPI because its threshold

*isaac.suarez@uv.es

†juan.mtnez.pastor@uv.es

takes place at very high excitation densities where the photogenerated carrier density is $N \sim 10^{18}\,\mathrm{cm}^{-3}$, one order of magnitude higher than the Mott transition carrier density, $N \sim 10^{17}\ \mathrm{cm}^{-3}$ [15,31–34]. On the other hand, reported values of the exciton binding energy of MAPI are particularly high at low temperatures (orthorhombic phase) [15]. Although they are reduced to 6–12 meV at room temperature [26,32,33], exciton recombination is usually considered dominating given their finite density of states, as compared to the case of free carriers where the density of states goes to zero at the bandgap energy. In addition, the ASE peak in MAPI is usually redshifted from the PL band and presents a superlinear dependence with the excitation fluence, which are characteristic of exciton-exciton or exciton-phonon scattering mechanisms [34], proposed to explain the optical gain in ZnO [35] or GaN [36] semiconductors. Indeed, different exciton scattering mechanisms have already been proposed to explain the lasing action in $CsPbBr_3$ perovskite microcavities [9,18] and nanowires [33]. Furthermore, it is possible to get ASE and lasing conditions below the Mott density, which opens new routes for photonics [35].

Taking into account these considerations, in the present work we focus on the interpretation of the PL spectra of polycrystalline MAPI layers at room T in terms of exciton and band-to-band emission [29–31], as the basis to understand the origin of ASE. For this purpose, we investigate the evolution of the PL spectra with the extication fluence of polycrystalline layers of MAPI integrated in polymer planar waveguides. We have already demonstrated that this configuration is an optimal one for ASE, because it provides a long path for the emitted photons and highly confines the optical modes of the photonic structure [11,12]. Here, we establish how the geometrical parameters influence the behavior of the waveguide to minimize the ASE threshold. We demonstrate that the ASE threshold (20–100 $\mathrm{W/cm}^2$ in our system) is achieved for excitation densities below the Mott density, hence the population of excitons would play a major role in the generation of optical gain. These experimental considerations are used as input parameters of a set of rate equations that result in a model able to reproduce the generation of optical gain in MHP films. Furthermore, we describe mathematically the light-emission signal and the excitation beam propagating along the planar optical waveguide, both incorporated into a beam-propagation method (BPM). Our simulations seem reasonably realistic, because they nicely reproduce the experimental results obtained in MAPI waveguides by fitting optical-gain parameters (threshold, gain coefficient, gain saturation, ...), indicating the validity of the proposed model. Finally, this work provides an understanding of the physical mechanisms underlying the ASE process in MAPI films, other than a useful tool to design active photonic devices with different architectures.

II. EXPERIMENTAL DETAILS AND WAVEGUIDE DESIGN

A. Experimental methods

$CH_3NH_3PbI_3$ layers are deposited on SiO_2/Si (2 μm of SiO_2) by using an intermediate 40-nm TiO_2 layer to improve the adhesion (details of the method are explained elsewhere [11]). Once the MAPI is properly grown on the substrate, a PMMA film is spin coated on top of the sample and post heated at 80 and 150 °C for 2 min. Here, the thicknesses of MAPI (d_1) and PMMA (d_2) films are ranged between $d_1 = 0.1$, 0.27 and 0.5 μm, and $d_2 = 0$, 0.5 and 2.5 μm, respectively. For this purpose, the thickness is controlled by the spin-coating velocity and/or the concentration of the species in the solvent. Finally, edges of the samples are cleaved for end fire-coupling purposes.

Waveguides are characterized by end fire coupling a Nd:YAG laser (1-ns pulse, 20-kHz repetition rate, doubled to 532 nm) at the input edge of the sample with the aid of a 40× microscope objective mounted on an *XYZ* stage. Intensity of the excitation beam is controlled by neutral density filters. Thus, the excitation fluence absorbed by the MAPI is ranged between 0 and 15 nJ per pulse within the waveguide geometry. Waveguided PL is collected at the output edge of the sample with a 20× microscope objective, also mounted on an *XYZ* stage. This PL signal, after traversing a 550-nm long-pass filter, is focused into an optical fiber (200-μm core) by using a cylindrical lens and connecting the fiber to a HR4000 Ocean Optics spectrograph (estimated overall resolution better than 0.7 nm). Time-resolved PL (TRPL) is carried out by focusing the PL from an optical fiber into a Hamamatsu C5658-3769 avalanche photodetector connected to a BOXCAR DPCS-150 electronics from Becker & Hickl GmbH. Figure 1 shows the main components of the experimental setup and the illustration of the waveguide structure.

A multilayer algorithm [36] is used to calculate the propagating modes confined in both the transverse electric (TE) and transverse magnetic (TM) polarizations at 532 nm (excitation wavelength) and 785 nm (PL wavelength). For these calculations, the refractive indices for Si, SiO_2, and PMMA are directly obtained from Palik [37], whereas the refractive index of TiO_2 is multiplied by 0.8 to take into account its porosity (see annex 1). Finally, the refractive index and absorption coefficient of the MHP layer is obtained from the results published elsewhere [9,38].

B. Design of optical waveguides

The waveguide configuration used in this work consists of a PMMA-MAPI bilayer deposited on a SiO_2/Si substrate (2 μm of SiO_2), as illustrated in Fig. 1. This design was proposed earlier and demonstrated an efficient optical amplification with better performances than other geometries (i.e., back scattering or excitation by variable

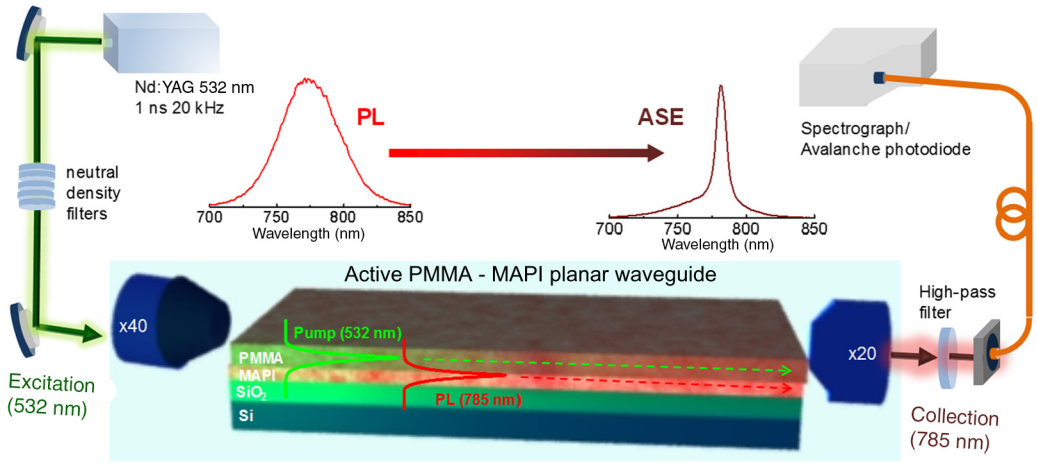

FIG. 1. Scheme of the sample structure and the experimental setup.

stripe-length method) [11,12]. In particular, this structure is based on the refractive-index contrast between the MAPI core ($n \approx 2.3$) and the SiO_2 ($n \approx 1.45$) bottom and the PMMA ($n \approx 1.49$) top claddings (see annex 1) to copropagate the PL and the pump beams along the entire length of the device (1–3 mm). Firstly, the PL at 785 nm is strongly confined in the MAPI film (red line in Fig. 1), which guarantees that emitted photons have a preferred directionality overlapping the active material. Secondly, the pump beam at 532 nm, which is end fire coupled at the input edge of the waveguide, propagates with low losses through cladding modes confined in the PMMA (green line in Fig. 1). The variation of the geometrical parameters [see Fig. 2(a)], i.e., thickness of the MAPI (d_1) and the PMMA (d_2), allows us to engineer the number of modes and their propagation constants at a specific wavelength. In particular, the pump beam at 532 nm mainly populates the TE_4 (TM_4) mode centered in the PMMA, while the PL goes through the TE_0 (TM_0) mode [red line in Fig. 2(a)] confined in the MAPI film. In fact, the MAPI can support from 1 to 4 propagating modes in both TE and TM polarizations for d_1 of 100 to 500 nm, respectively. On the one hand, high absorption losses at wavelengths shorter than the MAPI bandgap which is approximately equal to 1.63 eV (760 nm) inhibit the propagation of the excitation beam at 532 nm through these modes [$\alpha > 10\ \mu m^{-1}$ for TE_{0-3} (TM_{0-3}) at 532 nm, as observed in Fig. 2(b)]. On the other hand, the PMMA capping layer (with $d_2 > 0.75\ \mu m$) also allows the propagation of cladding modes (TE_4 and TM_4 and higher orders at 532 nm) with an effective refractive index of 1.47–1.49 and losses smaller than $\alpha = 0.1\ \mu m^{-1}$ that decrease with d_2 [green lines in Fig. 2(b)].

Consequently, the semiconductor film can be pumped along the whole length of the waveguide (1–3 mm) by the tail of this mode overlapping the MAPI film. Here, it is important to calculate the overlap of the modes (Γ) within the MAPI film by the following expression:

$$\Gamma = \frac{\int_{d_2}^{d_1+d_2} S_j(x)dx}{\int_{-\infty}^{\infty} S_j(x)dx}, \quad (1)$$

where $S_j(x)$ is the pointing vector of the mode j. In the case of the TE_4 mode at $\lambda = 532$ nm Eq. (1) indicates the fraction of the evanescent tail over the total mode distribution and ranges Γ_{TE4} between 0.02% and 0.15% [see black line in Fig. 2(b)]. At the same time, PL at 785 nm is efficiently coupled to the TE_{0-2} (TM_{0-2}) mode supported by the MAPI core, where the reabsorption losses will not be a problem above the ASE threshold. These modes present a real part of N_{eff} (N_{eff} is the effective refractive index of the mode) ranged between 1.5 and 2.25 [see Fig. 2(c)], a reduced attenuation at 785 nm in the order of $\alpha = 0.1$–$0.8\ \mu m^{-1}$, and are highly confined within the semiconductor film (Γ_{TE0-2} at 785 nm is higher than 90%).

III. OBSERVATION OF ASE IN PMMA-MAPI OPTICAL WAVEGUIDES

A. Influence of geometrical parameters on ASE

Figures 3(a)–3(c) show waveguided PL spectra at different excitation energies (0.15–15 nJ per pulse inside the waveguide considering 10% coupling efficiency) for three planar waveguides with $d_1/d_2 = 0.1/0.5$, 0.27/0.5, and 0.5/2.5 (all in μm). All figures present the same Y scale in order to compare their PL intensities. Clearly, geometrical parameters of the structure critically influence the generation and propagation of emitted light. For the thinnest MAPI and PMMA layers, $d_1/d_2 = 0.1/0.5$, PL collected at the output of the waveguide grows linearly with the excitation energy without any signature of optical amplification [Fig. 3(a)]. For MAPI layers with $d_1 = 0.27$ and $d_2 = 0.5$ PL collapses into a narrow peak

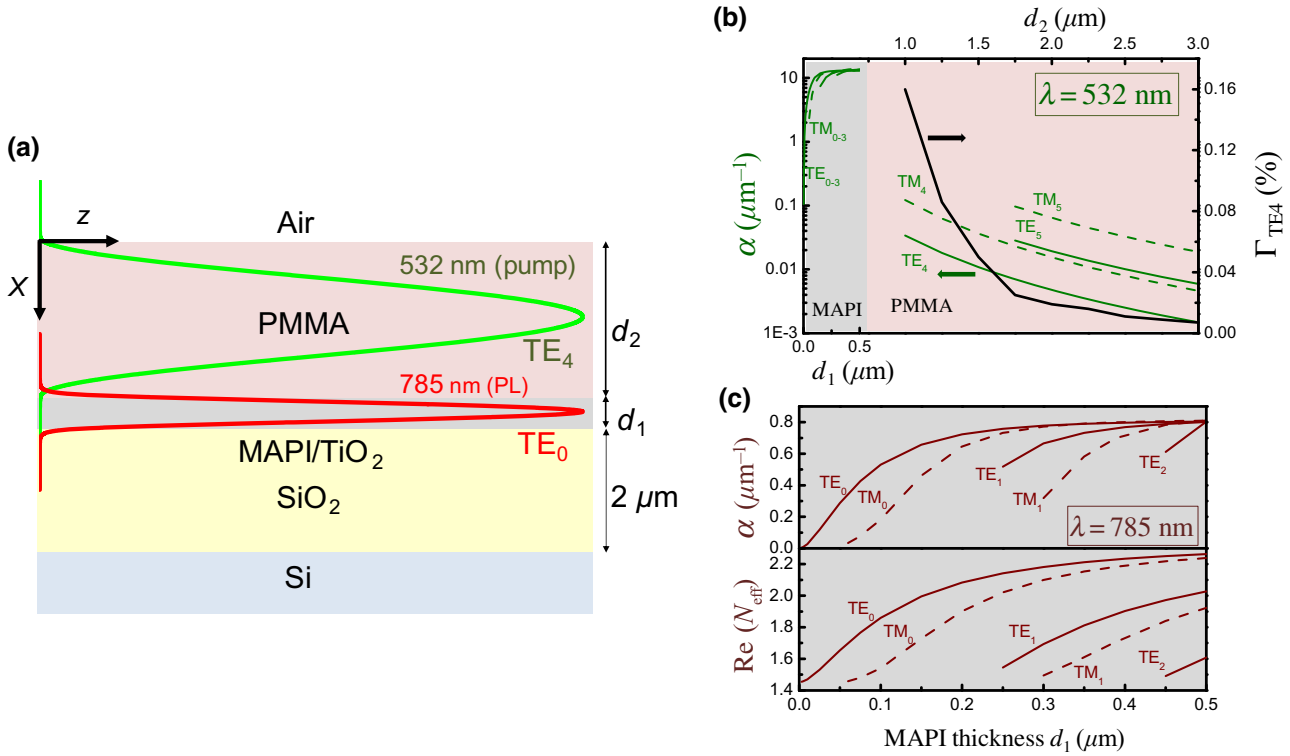

FIG. 2. (a) Structure of the waveguide and mode distribution for the TE_0 and TE_4 modes (TM modes demonstrate similar distribution) at 785 nm (PL) and 532 nm (excitation), respectively. The modes are calculated for a waveguide with $d_1 = 0.5$ μm and $d_2 = 2.5$ μm. (b) Analysis of the losses (left axis) and the confinement factor (right) along the structure as a function of the MAPI (d_1) and cladding (d_2) thicknesses at the pump wavelength (532 nm). Modes TE_{0-3} (TM_{0-3}) are weakly dependent on d_2 (because they are highly confined in the MAPI) and therefore only their dependence on d_1 is shown in the left part of the Fig. (bottom X axis); and modes TE_{4-6} (TM_{4-6}) are calculated for $d_1 = 0.5$ μm. The green lines refer to the absorption coefficient and the black line corresponds to the overlap of the mode within a MAPI film of $d_1 = 0.5$ μm. (c) Analysis of the propagating modes as a function of the MAPI film thickness (d_1) at PL wavelength (785 nm).

above a certain excitation fluence, which is a clear signature of ASE [Figs. 3(b)–3(c)]. Indeed, the geometrical parameters $d_1/d_2 = 0.5/2.5$ are optimum for ASE generation [Fig. 3(c)] from the point of view of the ASE threshold (E_{th}) and linewidth ($\Delta\lambda$), as shown in Fig. 3(d) and Table I. In this way, our results demonstrate that both $\Delta\lambda$ and E_{th} parameters decrease by increasing d_1 (>0.1 μm) in order to generate the required optical gain to overcome the parasitic losses of the waveguide and propagate the TE_0 (TM_0) mode at 785 nm confined in the MAPI film. At the same time, the optimum value of $d_2 = 2.5$ μm is a good compromise between the overlap of the evanescent tail of the TE_4 mode at 532 nm with the active material and its propagation losses [see Fig. 2(b)]. For the optimum geometrical parameters of the waveguide with $d_1/d_2 = 0.5/2.5$ we obtain $E_{th} \approx 2$ nJ and the ASE linewidth $\Delta\lambda \approx 3$ nm. Finally, such a specific method of optical pumping, based on the tail of the TE_4 mode traveling along the PMMA cladding layer, provides a quasiuniform excitation of the MAPI layer over the whole length of the waveguide (mm scale). Moreover, since the whole MAPI film is excited, the PL reabsorption effect, which is a well-known issue in MHP layers [39,40], is minimized with this scheme, even below the ASE threshold. Indeed, a study of ASE in waveguides of different lengths reveals that the reabsorption-induced redshift of the PL line is only 10 meV (5 nm) for the longest (3 mm) waveguides, as observed in Fig. 3(e), while for the case of PL measured in backscattering geometry the redshift can be as high as 25 nm for only 50-μm-thick MAPI film [39].

B. Analysis of spontaneous emission and ASE spectra

In agreement with the results reported in the literature [9,38,41], the absorption spectrum of MAPI film exhibits a sharp edge in the range of 1.60–1.65 eV [Fig. 4(a)], which is a characteristic of a direct bandgap semiconductor [42]. The experimental absorption spectrum [symbols in Fig. 4(a)] can be accounted by the Elliot theory, mainly taking into account the 1s exciton resonance [brown line in Fig. 4(a)] and the enhanced absorption at the exciton continuum [dark yellow line in Fig. 4(a)], in this case using the formula given elsewhere [43]. Indeed, according to previous publications [41,44] the exciton binding energy (R_y^*) in MAPI was found to be in the range of

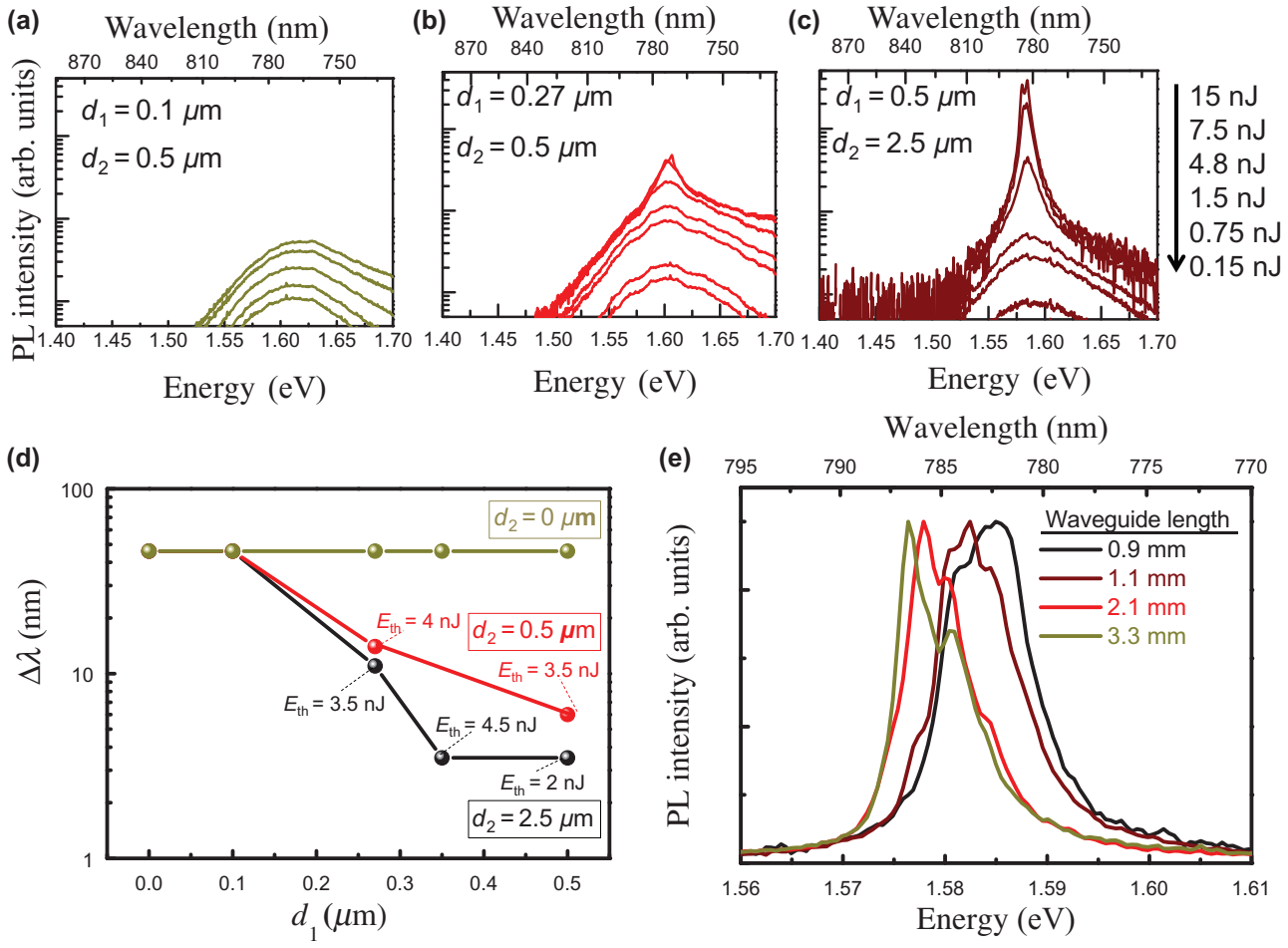

FIG. 3. PL spectra collected at the output edge of the waveguide for different excitation fluencies and geometrical parameters: (a) $d_1/d_2 = 0.1\ \mu$m/0.5 μm; (b) $d_1/d_2 = 0.27\ \mu$m/0.5 μm; (c) $d_1/d_2 = 0.5\ \mu$m/2.5 μm. Note that vertical axis presents the same scale to compare PL intensities. (d) PL linewidth, $\Delta\lambda$, as a function of MAPI thickness, d_1, using the PMMA thickness, d_2, as a parameter (the ASE threshold value is indicated for each case). (d) ASE spectra measured well above threshold in the waveguide with $d_1/d_2 = 0.5\ \mu$m/2.5 μm for different waveguide lengths.

6–37 meV, depending on temperature. In the case of our own experimental data in Fig. 4(a), the best fitting parameters are $E_g = 1.643$ eV, $(R_y^*) \approx 12.5$ meV (with an excitonic linewidth of around 30 meV), which is consistent with a similar fitting procedure to experimental results in the temperature range of 150–300 K (tetragonal phase of MAPI) [45].

Similarly to the case of the absorption spectrum, PL spectra (waveguided) also consist of two components ascribed to exciton and free-carrier recombination, both populations being in thermal equilibrium at room temperature according to Saha's equation [28], as schematically illustrated in Fig. 4(b). The PL spectrum measured under very low excitation energies (32 pJ) at the output edge

TABLE I. Summary of results obtained for perovskite waveguides in this work.

	$d_2 = 0\ \mu$m	$d_2 = 0.5\ \mu$m	$d_2 = 1\ \mu$m	$d_2 = 2.5\ \mu$m	$d_2 = 3.5\ \mu$m
$d_1 = 0.5\ \mu$m	no ASE	$E_{th} = 4$–5 nJ $\Delta\lambda \approx 6$ nm	$E_{th} = 3$–4 nJ $\Delta\lambda \approx 3.5$ nm	$E_{th} = 2$ nJ $\Delta\lambda \approx 3.5$ nm	–
$d_1 = 0.35\ \mu$m	no ASE	–	–	$E_{th} = 4$–5 nJ $\Delta\lambda \approx 3.5$ nm	$E_{th} = 4$–5 nJ $\Delta\lambda \approx 3.5$ nm
$d_1 = 0.27\ \mu$m	no ASE	$E_{th} = 4$ nJ $\Delta\lambda \approx 14$ nm	$E_{th} = 4$ nJ $\Delta\lambda \approx 14$ nm	$E_{th} = 3$–4 nJ $\Delta\lambda \approx 11$ nm	–
$d_1 = 0.1\ \mu$m	no ASE	no ASE	no ASE	no ASE	–

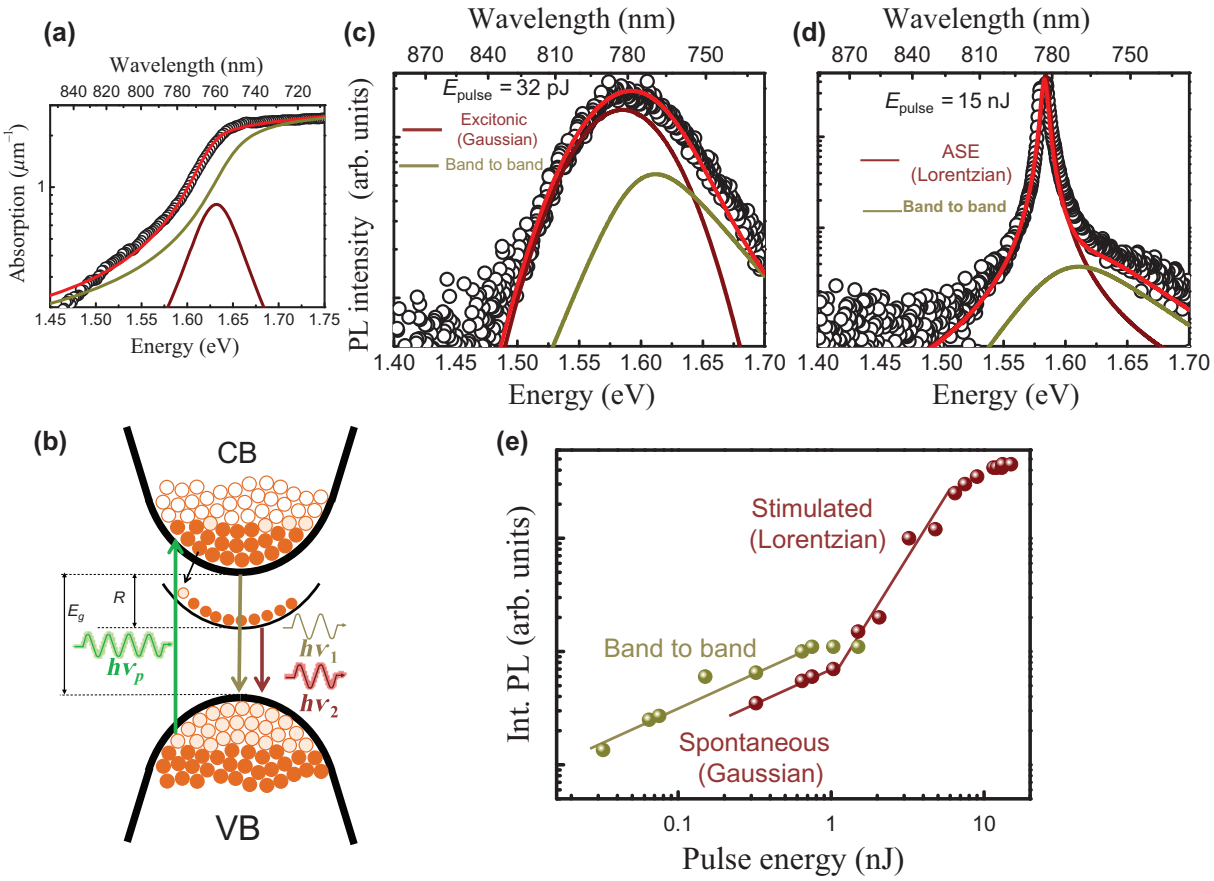

FIG. 4. (a) Absorption of $CH_3NH_3PbI_3$ perovskite films used in this work. (b) Mechanisms of the absorption and emission spectra formation. (c), (d) PL spectra measured at the output edge of the waveguide under low (32 pJ) (c) and high (15 nJ) (d) excitation energies. For low pump energy the spectra can be modeled (red line) by a sum of the spontaneous excitonic (Gaussian profile, brown line) and band-to-band (dark yellow line) optical transitions. Above a certain threshold the spontaneous PL spectrum collapses to a narrow peak that can be fitted by a Lorentzian line [brown line in (d)]. Symbols correspond to experimental data and solid lines to the fitting curves. (e) Integrated PL intensity of the spontaneous emission (Gaussian contour) and ASE band (Lorentzian contour) as a function of the excitation fluence (pulse energy).

of the waveguide fabricated with $d_1/d_2 = 0.5$ μm/2.5 μm [open symbols in Fig. 4(c)] is centered at 775 nm (1.6 eV) with a FWHM of 47 nm (95 meV). Similar spectra were measured under backscattering geometry in other publications [9,12,41] and hence ascribed to the spontaneous emission spectra in MAPI. The PL spectrum demonstrates an asymmetric shape with a less steep slope on the high-energy side, contrary to what would be expected from the PL reabsorption effect [46]. As aforementioned, we propose that waveguided PL spectra [data symbols in Fig. 4(c)] are formed by two contributions as earlier proposed for GaAs and GaN semiconductors [46–48]:

(i) the excitonic recombination f_X with Gaussian shape [brown line in Fig. 4(c)],

$$f_X = \frac{A_X}{\omega_X \sqrt{\pi/2}} e^{-2[(E-E_X)/w_X]^2} \tag{2}$$

and (ii) the excitonic continuum or band-to-band optical transition f_{BB} [dark yellow line in Fig. 4(c)] that contains the Maxwell-Boltzmann thermal tail:

$$f_{\mathrm{BB}} = \frac{A_{\mathrm{BB}}}{1 + e^{-(E-E_{\mathrm{BB}})/2\omega_{\mathrm{BB}}}} \times \frac{2}{1 + e^{-2\pi\sqrt{\frac{R}{E-E_{\mathrm{BB}}}}}} e^{-(E-E_{\mathrm{BB}})/E_t}, \tag{3}$$

where X and BB refer to the excitonic and band-to-band optical transitions, respectively; E_i, ω_i, and A_i ($i = X$, BB) are their corresponding emission energy, linewidth, and integrated intensity; R is the exciton binding energy and E_t is a fitting parameter standing for the carrier temperature. The experimental PL spectrum can be nicely fitted [red line in Fig. 4(c)] by the two contours defined by Eqs. (2) and (3) with R fixed to 12.5 meV, as obtained from the fit of the absorption coefficient spectrum in Fig. 4(a), yielding $E_x = 1.593$ eV, $E_{\mathrm{BB}} = E_x + R$, $E_t = 50$ meV, $\omega_X = 75$ meV, and $\omega_{\mathrm{BB}} = 10$ meV. Despite

the relatively low exciton binding energy, as also occurs in GaAs at room temperature, where R is even smaller (2.5–4 meV) [43,48], the integrated intensity of the PL corresponding to the exciton recombination [brown line in Fig. 4(c)] always dominates over the band-to-band component [dark yellow line in Fig. 4(c)] due to the finite density of states in the first case. Similar analysis carried out on passivated $CH_3NH_3PbBr_3$ perovskite thin films also concluded that excitons play a major role in the PL spectrum, which is even underestimated by the population predicted by Saha's equation [28].

At very high excitation energies (15 nJ at the input edge of the same waveguide with $d_1/d_2 = 0.5$ μm/2.5 μm) we clearly observe an ASE spectrum at the waveguide output edge [symbols in Fig. 4(d)], which is mainly characterized by a Lorentzian contour [49]:

$$f_L = \frac{2A_L\omega_L}{\pi} \times \frac{1}{4(E - E_L)^2 + {\omega_L}^2}, \tag{4}$$

where E_L, ω_L, and A_L are the emission energy, linewidth, and integrated intensity, respectively. The best fitting of the ASE spectrum to Eq. (4) [brown line in Fig. 4(d)] is obtained for $E_L = 1.590$ eV, which is very close to the peak of the excitonic emission line deconvoluted in Fig. 4(c). It is worth noting that a band-to-band contribution [Eq. (3)] continues to be observed on the high-energy side, without any background of excitonic spontaneous emission, other than the ASE Lorentzian line. These findings indicate the important role of excitons in ASE instead of more dense phases, as the electron-hole plasma, whose trace is not observed in the spontaneous emission nor ASE spectra.

The ASE regime is characterized by a superlinear increase of A_L above the ASE threshold at excitation energies of 1–2 nJ, as shown in Fig. 4(e) (brown symbols), other than a narrowing of ω_L with the excitation fluence, from 20 meV (1 nJ) down to 6–7 meV (15 nJ). In contrast, below the ASE threshold, both the excitonic [brown symbols below E_{th} in Fig. 4(e)] and band-to-band [dark yellow symbols in Fig. 4(e)] contributions to the spontaneous emission spectrum remain sublinear (and negligible above 2 nJ). The observed saturation of A_L for high excitation energies (>10 nJ) can be explained by the activation of the Auger nonradiative losses under such relatively high laser pump densities [10,50].

The results from TRPL experiments in MAPI-based waveguides presented in Fig. 5(a) are consistent with the spectral data discussed above. The TRPL signal at excitation pulse energies below the ASE threshold (0.75 nJ) exhibits a biexponential decay with time constants of 0.85–1.1 and 8–10 ns in the 770–790 nm spectral region (maximum of the Lorentzian ASE band). In contrast, as long as the excitation pulse energy is increased, the PL kinetics measured in the same spectral region shortens and decreases down to about 0.13 ns for the highest excitation energy (15 nJ). Indeed, the ASE threshold energy of 2 nJ [Fig. 4(e)] is undoubtedly corroborated by this PL transient shortening at the ASE wavelengths. In the region out of the ASE line, the PL decay is much longer [see map in Fig. 5(b)], as for example at 750 nm where the PL transient is described by a biexponential kinetics with decay times of 0.25–0.35 and 8–10 ns. Clearly, out of the narrow wavelength diapason corresponding to ASE, emitted light corresponds to spontaneous-emission traces, as occurs at 750 nm, where band-to-band carrier recombination dominates.

IV. MODELING OF ASE IN PMMA-MAPI WAVEGUIDES

In this section we propose a universal rate-equation model to describe ASE in MAPI films considering the experimental data presented in the previous sections. Then, this model is incorporated into a BPM algorithm to simulate the propagation of emitted light in the waveguides analyzed in this work. Appendix A–D details how equations are deduced in this section of the manuscript.

A. Experimental considerations

The analysis of the experimental PL and TRPL presented in the previous section reveals that the ASE band maximum for MAPI films is observed at the center of the excitonic part of the PL spectrum. We believe therefore that, at the threshold conditions, ASE in MAPI is carried out by the recombination of single excitons. We

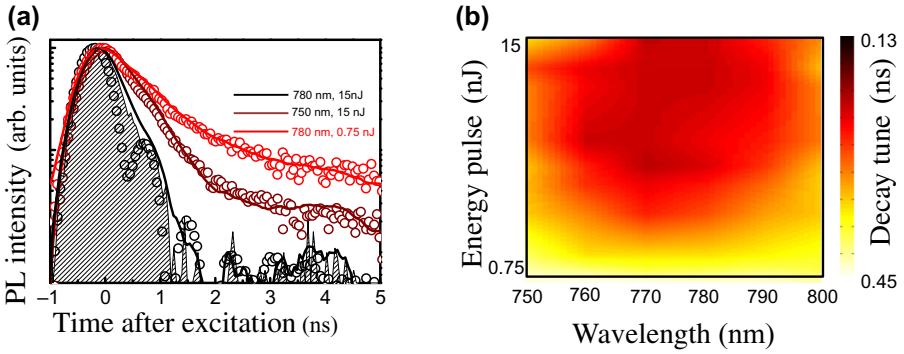

FIG. 5. (a) TRPL signals measured under low (red) and high (black and wine) excitation fluencies at 780 nm (red and black) and 750 nm (wine). Symbols, solid lines, and dashed area refer to experimental data, fitting curves, and the instrument response function, respectively. (b) PL decay time map of the faster decay component measured at the output edge of a MAPI-based waveguide.

can estimate the concentration of excitons (n_x) at the ASE threshold excitation fluence by considering the rate equation:

$$\frac{dn_x}{dt} = G - \frac{n_x}{\tau_r}, \tag{5}$$

where τ_r is the recombination time and G is the carrier generation rate, which is determined by light absorption (α), photon energy ($h\nu$), and excitation peak fluence (P/A) [42]:

$$G = \frac{P}{A \times h\nu}\alpha(h\nu). \tag{6}$$

Here, $\alpha(h\nu) = 13\times10^4$ cm^{-1} is obtained from the absorption spectrum shown in Fig. 4(a) at the excitation wavelength (532 nm), and $P/A = 20$–100 W/cm^2 is obtained from our experimental conditions (see Ref. [11] and Appendix A). On the basis of our TRPL measurements, we evaluate carrier recombination time at fluencies below the ASE threshold as $\tau_r \approx 3.5$ ns. Hence, following the formula (5), in the quasistationary regime within an excitation pulse, $n_x = G\ \tau_r \approx [2.4\text{–}12]\times10^{16}$ cm^{-3}, which is lower than the Mott carrier density reported for MAPI thin films (1×10^{18} cm^{-3}) [50], MAPI crystals (1×10^{18} cm^{-3}) [51], $CsPbBr_3$ nanocrystals (7×10^{17} cm^{-3}) [32], or $CH_3NH_3PbBr_3$ thin films (8×10^{17} cm^{-3}) [34]). This is further evidence, together with the above discussed waveguided emitted-light spectra, below and above the ASE threshold, that excitons are playing a major role in the origin of ASE, at least under excitation conditions not far from threshold conditions. Of course, if higher excitation fluencies (leading to carrier densities well above the Mott value) are needed to reach the ASE threshold, the role of free carriers would be dominant due to the Coulomb screening effect, which is the origin of the formation of a dense phase (e.g., the electron-hole plasma) [15].

B. Rate equations

In a conventional bulk semiconductor, the absorption of light [green vertical line in Fig. 6(a)] promotes the formation of a population of n_c electrons in the conduction band (CB) and p_v holes in the valence band (VB) with the corresponding shift of the quasi-Fermi levels E_{FC} and E_{FV} (see Appendix B) [42]. In these conditions, the most widely used rate-equation model typically includes carrier trapping (purple line), bimolecular radiative recombination (red line), and Auger recombination (dashed purple line) mechanisms with coefficients A, B, and C, respectively. This is known as the ABC model with $n = n_c = p_v$, $dn/dt = An - Bn^2 - Cn^3$, and it is usually chosen to analyze the recombination dynamics in MAPI films [50]. Moreover, this rate equation can incorporate the stimulated emission term $g(h\nu)\ S(h\nu)/h\nu$, where S and g are the photon density and optical gain at a given energy $h\nu$. Here, the photon propagation equation, $dS/dz = gS + kn$ (k is a constant related to the spontaneous emission), can be solved in parallel to determine S, whereas $g(h\nu)$ is given by [42]

$$g(h\nu) = \alpha(h\nu)(f_c - f_v), \tag{7}$$

where $\alpha(h\nu)$ is the absorption coefficient at the same energy, and $(f_c - f_v)$ is the difference between the occupation probabilities in CB (f_c) and VB (f_v) states differing an energy $h\nu$, and are calculated following to the procedure described in Appendix B.

Nevertheless, according to the above given reasoning, a model for gain in MAPI films should also include the generation of excitons [dark blue solid circles in Fig. 6(a)], the equilibrium between excitons and free carriers given by Saha's equation (see Appendix C) and the emission of a photon by the exciton radiative recombination [brown line in Fig. 6(a)]. The system is modeled by the four-level scheme presented in Fig. 6(b). As the semiconductor is optically pumped far above the bandgap ($h\nu_p \gg E_g$), an infinite reservoir (level $R>$) of electrons (holes) is considered to be available at the bottom (top) of the CB (VB).

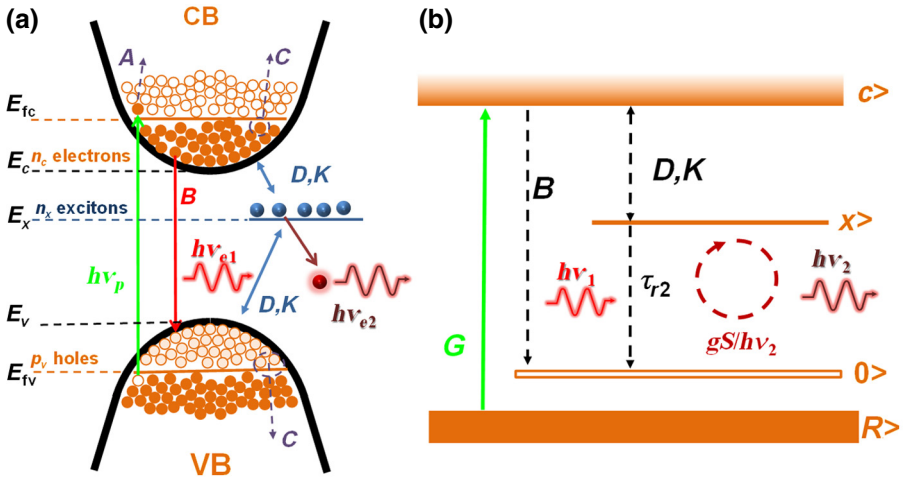

FIG. 6. (a) Band diagram and generation of light. E_{FC}, E_{FV} are the quasi-Fermi levels at the conduction and valence band, respectively. E_c, E_v, and E_x refer to the energy position of the bottom of the conduction band, top of the valence band and 1s excitonic level, respectively. (b) Amplification model based on the four-level scheme.

When MAPI is pumped at a rate G, n_c electrons populate the continuum level $C>$. If the same population is assumed for holes ($n_c = p_v$) and nonradiative channels are neglected ($A = C = 0$) or included in an effective recombination time, the electron-hole pairs can radiatively recombine to the ground state ($0>$) with the bimolecular recombination constant B or form excitons at a rate D. The exciton level ($X>$) is included with a population density n_x, which can radiatively recombine at the rate $1/\tau_{r2}$. In addition, excitons and free carriers are in thermal equilibrium, whose populations n_x and n_c are governed by the Saha equation that yields the coefficient K.

At these conditions, the following rate equations reproduce the scheme of Fig. 6(b):

$$\frac{dn_c}{dt} = G - Bn_c^2 - Dn_c^2 + DKn_X - \alpha_c \frac{S_c}{h\nu}(f_c - f_v), \quad (8)$$

$$\frac{dn_x}{dt} = Dn_c^2 - DKn_X - \frac{n_X}{\tau_r} - \alpha \frac{S}{h\nu}(2f_{\text{ex}} - 1). \quad (9)$$

Equations (8) and (9) contain the stimulated emission term for free carriers, $\alpha_c S_c(f_c - f_v)/h\nu$, and excitons, $\alpha S(2f_{\text{ex}} - 1)/h\nu$; where the occupation probability at the exciton level, f_{ex}, is explained in Appendix C, S is the photon flux and the subindex c refers to carriers. K is evaluated to be around 6.7×10^{17} cm^{-3}, which is not far from the Mott density reported for this material, as discussed above. Taking into account this value for K, the fact that the formation rate of excitons is much higher than radiative recombination $DK \gg B$ (see Appendix C for details), and neglecting the optical gain for free carriers, Eqs. (8) and (9) can be easily solved for the stationary regime, giving

$$G = \frac{n_X}{\tau_r} + \alpha \frac{S}{h\nu}(2f_{\text{ex}} - 1), \quad (10)$$

$$K = \frac{n_c^2}{n_x}. \quad (11)$$

C. Theoretical and experimental gain in MAPI films

The threshold of optical gain in a semiconductor is reached when $f_c = f_v = 0.5$, and can be calculated with the transparency condition (gain = losses) in a semiconductor [42]:

$$\tilde{F}_{1/2}\left(\frac{n_c}{N_c}\right) + \tilde{F}_{1/2}\left(\frac{p_v}{N_v}\right) = 0, \quad (12)$$

where $n_c = p_v$ is usually assumed, $\tilde{F}_{1/2}$ is the inverse function of the Fermi integral of order ½ and N_c (N_v) is the density of states in the CB (VB). For example, optical gain in GaAs reaches a value of 300 cm^{-1} at room temperature above the transparency carrier concentration N_0 (GaAs) $= 1.2\times10^{18}$ cm^{-3} [52]. For MAPI, $N_0 = (n_c = p_v =) \ 2.5\times10^{18}$ cm^{-3} after taking into account $m_e^* = 0.23m_0$ and $m_h^* = 0.29m_0$ [53]. Above this threshold, the material gain exhibits a linear variation with the carrier density [solid red line of Fig. 7(a)], and Eq. (7) can be approximated by

$$g_0 = \sigma(n_c - N_0). \quad (13)$$

The extraordinary gain in MAPI is clearly demonstrated with a large slope close to $\sigma = 3\times10^{-15}$ cm^2, as estimated through Eq. (13), and corroborates the potential applications of MAPI materials for optical amplifiers and lasers [7–11,13,54–60]. Indeed, although N_0 in MAPI is slightly higher than that obtained for GaAs or InP (solid green and blue lines in Fig. 7(a), respectively) [42], σ is enhanced by one order of magnitude, indicating the benefits of MHPs as an alternative to traditional III-V semiconductors, also because it can be easily integrated in different passive photonic platforms (Si, SiNx, flexible polymer, ...) [11,12].

The value of $N_0 = 2.5\times10^{18}$ cm^{-3} deduced in the previous section is in good agreement with some reported experimental results [15,31–33] and is very close to the Mott density reported for this material family (approximately equal to 10^{18} cm^{-3}) [32,34,50,51]. However, it is more than one order of magnitude higher than the exciton density threshold estimated above through Eqs. (5) and (6) (approximately equal to [2.4–12] $\times 10^{16}$ cm^{-3}). Therefore, it is reasonable to infer that excitons play a major role in the formation of optical gain, where ASE is obtained from the condition $f_{\text{ex}} = 0.5$.

D. Propagation equation

Finally, for the purpose of solving Eqs. (10) and (11) we take $\alpha(h\nu)$ from the experimental absorption coefficient spectrum shown in Fig. 4(a) as 0.8 μm^{-1} at the ASE wavelength and τ_r (the effective exciton recombination time) as $\tau_r = 3.5$ ns according to our TRPL measurements below the threshold fluence. Eqs. (10) and (11) must be solved together with the Maxwell equations in the photonic configuration under study in order to calculate the photon density, S. In the waveguide structure proposed in this work, this rate equation is incorporated into a BPM algorithm following the approximation developed elsewhere [15,31–33]. First of all, the algorithm simulates the propagation of the pump beam at 532 nm in order to evaluate the concentration of carriers photogenerated in the active material (G) at each propagation step. In particular, the algorithm predicts that more than 95% of the incoming light at 532 nm is coupled to the TE_4, and that this mode propagates with an attenuation of 0.003 μm^{-1} [green line in Fig. 7(b)]. In these conditions, the algorithm considers overlap of the tail of the mode with the active material to estimate G. Then, exciton (n_X) and carrier (n_c) concentrations are calculated at each propagation step by solving numerically Eqs. (10) and (11), and g is evaluated by using by $\alpha(2f_{\text{ex}} - 1)$. For

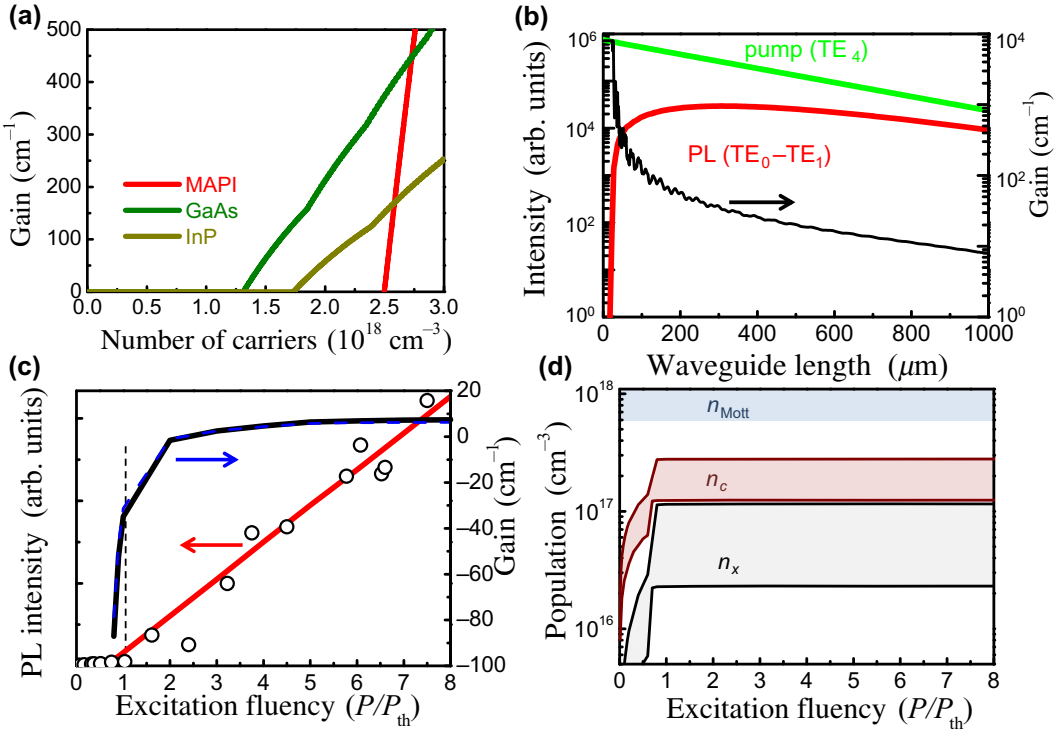

FIG. 7. (a) Gain of GaAs, InP, and MAPI materials. (b) Intensities of waveguided pump (solid green line) and PL (solid red line) beams above threshold ($10\times P_{th}$). Gain obtained with the model (black solid line). (c) Left axis: experimental (symbols) and calculated (solid red line) waveguided emitted light intensity as a function of the relative pump fluence (P/P_{th}). Right axis: gain obtained with the model (black solid line) at $z = 1000$ μm and approximated (dashed blue line) with Eq. (12) as a function of P/P_{th}. (d) Range of the population of excitons (red area) and free carriers (black area) as a function of the relative pump fluence (P/P_{th}). Blue area shows the range of the Mott density reported for perovskite families.

this purpose, f_{ex} is calculated by considering the exciton binding energy, 12.5 meV, and N_X as the carrier density at the ASE threshold ([2.4–12]) $\times 10^{16}$ cm^{-3}). Here, it is worth mentioning that, although the value of N_X impacts the simulated power density at the threshold (P_{th}), it does not influence the optical gain reached for a pump fluence larger than P_{th}. The evolution of g as a function of z for $10\times P_{th}$ is plotted in Fig. 7(b) (black line). The predicted peak gain at the beginning of the waveguide is generated by TE_{0-3} modes. However, since these modes are strongly attenuated for $z > 20$ μm, g follows the TE_4 intensity above this distance.

At these conditions, the spontaneous emission of MAPI is included in the BPM algorithm by considering an electrical current $J(x,y,v)$ different than zero in the Maxwell equation for a plane-wave electromagnetic field, which takes the following form for TE polarization (extension to TM is straightforward):

$$\nabla^2 E(x,y,z) + k^2 E(x,y,z) = i\omega\mu J(x,y,z), \qquad (14)$$

where E is the electric field, k the wave vector, ω the angular frequency, and μ the magnetic permeability. Here $J(x,y,v)$ is considered to depend on the excitonic generation $[n_x(x,y,z)]$ by

$$J(x,y,z) = \sqrt{\sigma n_x(x,y,z) E_s \Delta V}, \qquad (15)$$

where $E_s = h\nu$ is the energy of generated photons, ΔV the linewidth of the spontaneous emission (2×10^{13} s^{-1}) and σ the conductivity of the material in the range 10^{-7}–10^{-5} Ω^{-1} cm^{-1} [61]. The square root is included to preserve the right units in J (in A/cm^2). In addition, the imaginary part of the refractive index is evaluated at each propagation step in order to consider the optical gain. For this layer we also include losses of 20 cm^{-1} according to our previous studies in MAPI waveguides [11] or polymer layers containing colloidal quantum dots [62]. This attenuation can include the scattering in the polycrystalline grains or radiation leaving the waveguide from the surface. In particular, the BPM algorithm predicts the propagation of PL through the modes TE_0 and TE_1, whose intensity along the waveguide depends on the carrier generation. The red line in Fig. 7(b) depicts the PL intensity along the waveguide excited above threshold ($10\times P_{th}$). Signal shows a fast growth at the input edge of the waveguide

where the highest optical gain of 8000 cm^{-1} [see black line and right axis in Fig. 7(b)] is generated. Since the TE_0 and TE_1 modes at 785 nm are highly confined ($\Gamma \approx 1$) in the MAPI film, this gain corresponds to both material (g_m) and modal ($g = \Gamma \times g_m$) gains of the waveguide. Then, the signal level is so high that gain saturation [last term in Eq. (10)] inhibits the generation of carriers, and optical gain starts to decrease keeping a constant intensity of PL between $z = 200$–600 μm. For waveguide lengths $z > 600$ μm the intensity of the pump beam is not high enough to keep the maximum PL generation, and an intensity of the emitted light monotonically decreases with the length of the waveguide.

Simulations carried out at different excitation fluencies indicate an ASE threshold an order of magnitude higher than that observed experimentally. We believe that photonic geometry can benefit ASE by an additional reduction of the threshold. This effect is commonly observed in laser cavities (let us take into account that a planar waveguide would be a single-pass laser structure [63]), and it is included in Eq. (10) by a factor (1-β) multiplying the coefficient B, where β indicates the fraction of the spontaneous emission coupled to a given mode [63]. In particular, our experimental data on the PL intensity at 785 nm (symbols) is nicely reproduced with $\beta = 0.95$. At these conditions, the model predicts an increase of the optical gain [black line of Fig. 7(c)] with the excitation fluence (P), which is in agreement with the experimental data presented elsewhere [11]. Here, PL intensity and g are plotted at $z = 1000$ μm as a function of the relative power $P/P_{th.}$ This behavior can be modeled by considering a gain without saturation (g_0) obtained with Eq. (12) and a saturation intensity Ps [52]:

$$g = \frac{g_0}{1 + {}^{P}/_{P_s}}. \tag{16}$$

This approximation can effectively reproduce the gain curve with $g_0 = 250 \times 10^{-15}$ $(n_c - N_0)$ cm^{-1} and $P_s = 1$ μJ per pulse. In addition, it is interesting to say that the obtained value of $\sigma = 2.5 \times 10^{-15}$ cm^2 approaches that calculated in Fig. 6(a). According to the model, optical gain occurs when f_{ex} is higher than 0.5, or, in other words, when n_{ex} [black line in Fig. 7(d)] overcomes the transparency carrier density, $n_{x0} = 2.35 \times 10^{16}$–$1.15 \times 10^{17}$ cm^{-3} [dashed line in Fig. 7(d)]. Following Saha's equation, the corresponding population of free carriers (n_c) will be in the range $n_{c0} = 10^{17}$–3×10^{17} cm^{-3} [red region in Fig. 7(d)] at the threshold, which is below the transparency concentration of free carriers obtained from Eq. (11) (2.5×10^{18} cm^{-3}). This fact corroborates our assumption that excitons are needed to be considered for the optical gain. Finally, it is worth mentioning that the populations deduced in the modeling are well below the range of values for the Mott density reported for this MHP semiconductors [gray area in Fig. 7(d)].

V. CONCLUSIONS

In summary, in this work we have studied the generation of optical gain of MAPI integrated in polymer (PMMA) waveguides. Compared with other configurations (backscattering, surface excitation....), our waveguide structure provides necessary degrees of freedom to enhance the generation of optical gain. In particular, propagation constants of the modes are properly engineered by the geometrical parameters to minimize the ASE threshold (20–100 nJ/cm^2 for the best device). For this purpose, the waveguide allows the propagation of the excitation beam at 532 nm along the whole length of the waveguide cladding (PMMA) providing at the same time a high confinement for emitted photons at the waveguide core (MAPI). According to the results obtained for the waveguided PL below and above the ASE threshold, the stimulated emission originates at photogenerated carrier concentration below the Mott density value, which reveals the dominant role of excitons in the origin of ASE. On the basis of these findings, a rate-equation model is properly developed to calculate the occupancy of electron states in conduction and valence bands and excitons. Moreover, when this model is introduced in a BPM algorithm, the experimental results obtained for the investigated PMMA-MAPI waveguides are quantitatively reproduced. The advantages of this model rely not only on the extraction of the gain parameters (optical gain and ASE threshold), but also on an easy extension to other photonic structures and devices containing MHP or other active materials. Therefore, this work represents a useful tool towards the design of prospective active MHP devices.

ACKNOWLEDGMENTS

Financial support by Spanish MCINN through Project No. TEC2017-86102-C2-1-R and the National Network of Research Excellence No. ENE2017-90565-REDT, by the Generalitat Valenciana via the project Q-Devices (Prometeo/2018/098), by the University of Valencia via Project UV-INV-AE16-514545 and by the European Research Council (ERC) via Consolidator Grant (724424 - No-LIMIT) are gratefully acknowledged.

APPENDIX A: CALCULATION OF EXCITATION FLUENCE

Excitation fluence in the waveguides is estimated from the excitation pulse measured after the laser source at threshold 20 nJ, the overlap of the TE_4 mode with the active region (0.2×10^{-3}), the size of the mode and coupling efficiency. Since the structure is a planar waveguide, we consider an elliptical mode distribution of 1.25×50 μm^2 at the input edge of the waveguide estimated from the thickness of the PMMA and the recorded scattering from the surface of the sample. Propagation of

the beam along the planar structure results in the diffraction of the mode, which reaches about $1.25 \times 500\ \mu m^2$ for $z = 1$ mm. Concerning the coupling efficiency, it must consider the Fresnel reflection in the input objective and the sample (about 40% is reflected), the difference between the input beam and the propagation mode and the misalignments. In these conditions, we believe that is not possible to obtain a coupling efficiency higher than 10%, and we use 1%–5% for our calculations.

APPENDIX B: CALCULATION OF OCCUPATION PROBABILITIES

The absorption of light in a semiconductor [green vertical line in a sketch in Fig. 6(a)] produces the promotion of electrons from the VB to the CB.

$$E_{FC} = E_c + kT \times \tilde{F}_{1/2}\left(\frac{n_c}{N_c}\right),$$

$$E_{FV} = E_v - kT \times \tilde{F}_{1/2}\left(\frac{p_v}{N_V}\right),$$

where E_c (E_v) is the bottom (top) of the conduction (valence) band, k is the Boltzmann constant, T is the temperature, $\tilde{F}_{1/2}$ is the inverse function of the Fermi integral of order ½ and N_c (N_v) is the density of states in the CB (VB), respectively:

$$F_{1/2}(u) = \frac{1}{\Gamma(1/2)}\int_0^\infty \frac{x^{1/2}}{1+e^{(x-u)}}dx,$$

$$N_c = \frac{1}{4}\left(\frac{2m_e^* \times kT}{\pi\hbar^2}\right)^{3/2},$$

$$N_v = \frac{1}{4}\left(\frac{2m_h^* \times kT}{\pi\hbar^2}\right)^{3/2},$$

where $\hbar$ is the reduced Planck constant and m_e^* (m_h^*) is the electron (hole) effective mass. In these conditions, the probability that the state of energy $E_c(h\nu)$ [$E_v(h\nu)$] of the CB (VB) would be occupied obeys the Fermi distribution:

$$f_c(h\nu) = \frac{1}{1+\exp\{[Ec(h\nu) - E_{FC}]/kT\}},$$

$$f_v(h\nu) = \frac{1}{1+\exp\{[Ev(h\nu) - E_{FV}]/kT\}}.$$

Accordingly, $E_c(h\nu)$ and $E_v(h\nu)$ are related to the bandgap energy (E_g) and the reduced effective mass (m_r) by the relations:

$$E_c(h\nu) = E_g + \frac{m_r}{m_e^*}(h\nu - E_g),$$

$$E_v(h\nu) = -\frac{m_r}{m_h^*}(h\nu - E_g).$$

APPENDIX C: OCCUPATION PROBABILITY IN EXCITONS AND SAHA'S EQUATION

Following the approximation proposed elsewhere [35], the occupation probability of excitons obeys the equation

$$f_{ex}(h\nu) = \frac{1}{1+\exp\{[E(h\nu) - \mu]/kT\}},$$

where $E(h\nu)$ is fixed at -12.5 meV (experimental exciton binding energy) with respect to the bottom of the CB and μ is the chemical potential given by

$$\mu = kT \times \ln\left(e^{n_x/N_x} - 1\right),$$

where N_x is the exciton population at the threshold of stimulated emission, ranged between 2.4×1016 cm^{-3} and 1.2×1017 cm^{-3}, according to our experimental results (Sec IV.A).

On the other hand, the equilibrium population K between free carriers and excitons is given by the Saha equation:

$$K = \frac{n_c^2}{n_x} = \left(\frac{2\pi\mu kT}{h}\right)^{3/2} e^{-R_y/kT}$$

from which $K = 6.7\times10^{17}$ cm^{-3}. On the other hand, $B = (N_0\tau_{eff})^{-1} = 5\times10^{-11}$ s^{-1} cm^3, where τ_{eff} is the effective recombination time, set to $\tau_{eff} = 8$ ns, as measured in backscattering geometry under very low excitation conditions [11]. According to data published by other authors [64], B ranges between 2×10^{-11} and 1.4×10^{-10} cm^3 s^{-1}, so we believe that our assumptions above provides realistic results. Finally, D can be calculated as $1/N_0\tau_f$, where τ_f is a formation time for excitons (approximately 1 fs), and hence $D = 10^{-4}$ cm^{-3} s^{-1}, in agreement with experimental data reported by other authors [28]. In these conditions, $DK \gg B$.

APPENDIX D

Given the large number of parameters, magnitudes, and their corresponding symbols used in this section, we compile all of them in Ref. [65], for a reader to use it for consultation if necessary.

[1] Z. Shi and A. H. Jayatissa, Perovskites-based solar cells: A review of recent progress, materials and processing methods, Materials (Basel) **11**, 729 (2018).
[2] Q. Fu, X. Tang, B. Huang, T. Hu, L. Tan, L. Chen, and Y. Chen, Recent progress on the long-term stability of perovskite solar cells, Adv. Sci. **5**, 1700387 (2018).
[3] A. K. Jena, A. Kulkarni, and T. Miyasaka, Halide perovskite photovoltaics: Background, status, and future prospects, Chem. Rev. **119**, 3036 (2019).

[4] A. Fakharuddin, L. Schmidt-Mende, G. Garcia-Belmonte, R. Jose, and I. Mora-Sero, Interfaces in perovskite solar cells, Adv. Energy Mater. **7**, 1700623 (2017).

[5] T. P. White, E. Deleporte, and T. C. Sum, Feature issue introduction: Halide perovskites for optoelectronics, Opt. Express **26**, A153 (2018).

[6] A. Fakharuddin, U. Shabbir, W. Qiu, T. Iqbal, M. Sultan, P. Heremans, and L. Schmidt-Mende, Inorganic and layered perovskites for optoelectronic devices, Adv. Mater. **31**, 1807095 (2019).

[7] T. T. Ngo, I. Suarez, G. Antonicelli, D. Cortizo-Lacalle, J. P. Martinez-Pastor, A. Mateo-Alonso, and I. Mora-Sero, Enhancement of the performance of perovskite solar cells, LEDs, and optical amplifiers by anti-solvent additive deposition, Adv. Mater. **29**, 1604056 (2017).

[8] B. R. Sutherland and E. H. Sargent, Perovskite photonic sources, Nat. Photonics **10**, 295 (2016).

[9] G. Xing, N. Mathews, S. S. Lim, N. Yantara, X. Liu, D. Sabba, M. Grätzel, S. Mhaisalkar, and T. C. Sum, Low-temperature solution-processed wavelength-tunable perovskites for lasing, Nat. Mater. **13**, 476 (2014).

[10] I. Suárez, Active photonic devices based on colloidal semiconductor nanocrystals and organometallic halide perovskites, Eur. Phys. J. Appl. Phys. **75**, 30001 (2016).

[11] I. Suárez, E. J. Juárez-Pérez, J. Bisquert, I. Mora-Seró, and J. P. Martínez-Pastor, Polymer/perovskite amplifying waveguides for active hybrid silicon photonics, Adv. Mater. **27**, 6157 (2015).

[12] I. Suárez, E. Hassanabadi, A. Maulu, N. Carlino, C. A. Maestri, M. Latifi, P. Bettotti, I. Mora-Seró, and J. P. Martínez-Pastor, Integrated optical amplifier–photodetector on a wearable nanocellulose substrate, Adv. Opt. Mater. **6**, 1800201 (2018).

[13] B. R. Sutherland, S. Hoogland, M. M. Adachi, C. T. O. Wong, E. H. Sargent, and S. E. T. Al, Conformal organohalide perovskites enable lasing on spherical resonators, ACS Nano **8**, 10947 (2014).

[14] S. Chen, K. Roh, J. Lee, W. K. Chong, Y. Lu, N. Mathews, T. C. Sum, and A. Nurmikko, A photonic crystal laser from solution based organo-lead iodide perovskite thin films, ACS Nano **10**, 3959 (2016).

[15] Y. Jia, R. A. Kerner, A. J. Grede, A. N. Brigeman, B. P. Rand, and N. C. Giebink, Diode-pumped organo-lead halide perovskite lasing in a metal-clad distributed feedback resonator, Nano Lett. **16**, 4624 (2016).

[16] X. F. Liu, S. T. Ha, Q. Zhang, M. de la Mata, C. Magen, J. Arbiol, T. C. Sum, and Q. H. Xiong, Whispering gallery mode lasing from hexagonal shaped layered lead iodide crystals, ACS Nano **9**, 687 (2015).

[17] Q. Wang, K. Sun, W. Li, J. Gu, Z. Xiao, and S. Song, Unidirectional lasing emissions from $CH_3NH_3PbBr_3$ perovskite microdisks ACS, Photonics **3**, 1125 (2016).

[18] Q. Zhang, S. T. Ha, X. Liu, T. C. Sum, and Q. Xiong, Room-temperature near-infrared high-Q perovskite whispering-gallery planar nanolasers, Nano Lett. **14**, 5995 (2014).

[19] H. Zhu, Y. Fu, F. Meng, X. Wu, Z. Gong, Q. Ding, M. V. Gustafsson, M. T. Trinh, S. Jin, and X. Y. Zhu, Lead halide perovskite nanowire lasers with low lasing thresholds and high quality factors, Nat. Mater. **14**, 636 (2015).

[20] J. Xing, X. Liu, Q. Zhang, S. T. Ha, Y. Yuan, C. Shen, T. C. Sum, and Q. Xiong, Vapor phase synthesis of organometal halide perovskite nanowires for tunable room-temperature nanolasers, Nano Lett. **15**, 4571 (2015).

[21] Y. Jia, R. A. Kerner, A. J. Grede, B. P. Rand, and N. C. Giebink, Continuous-wave lasing in an organic-inorganic lead halide perovskite semiconductor, Nat. Photonics **11**, 784 (2017).

[22] P. Brenner, O. Bar-on, M. Jakoby, I. Allegro, B. S. Richards, U. W. Paetzold, I. A. Howard, J. Scheuer, and U. Lemmer, Continuous wave amplified spontaneous emission in Phase-Stable Lead Halide Perovskites, Nat. Commun. **10**, 988 (2019).

[23] Z. Li, J. Moon, A. Gharajeh, R. Haroldson, R. Hawkins, W. Hu, A. Zakhidov, and Q. Gu, Room-Temperature continuous-wave operation of organometal halide perovskite lasers, ACS Nano **12**, 10968 (2018).

[24] V. S. Chirvony, S. González-Carrero, I. Suárez, R. E. Galian, M. Sessolo, H. J. Bolink, J. P. Martínez-Pastor, and J. Pérez-Prieto, Delayed luminescence in lead halide perovskite nanocrystals, J. Phys. Chem. C **121**, 13381 (2017).

[25] V. S. Chirvony and J. P. Martínez-Pastor, Trap-Limited dynamics of excited carriers and interpretation of the photoluminescence decay kinetics in metal halide perovskites, J. Phys. Chem. Lett. **9**, 4955 (2018).

[26] M. Saba, F. Quochi, A. Mura, and G. Bongiovanni, Excited state properties of hybrid perovskites, Acc. Chem. Res. **49**, 166 (2016).

[27] W. K. Chong, K. Thirumal, D. Giovanni, T. W. Goh, X. Liu, N. Mathews, S. G. Mhaisalkar, and T. C. Sum, Dominant factors limiting optical gain in layered two-dimensional halide perovskites thin films, Phys. Chem. Chem. Phys. **18**, 14701 (2016).

[28] F. Mariano, A. Cretì, L. Carbone, A. Genco, S. D'Agostino, S. Carallo, G. Montagna, M. Lomascolo, and M. Mazzeo, The enhancement of excitonic emission crossing Saha equilibrium in trap passivated $CH_3NH_3PbBr_3$ perovskite, Commun. Phys. **3**, 1 (2020).

[29] Claus Klingshirn, *Semiconductor Optics* (Springer, New York, 2005).

[30] K. Asano and T. Yoshioka, Exciton – mott physics in two-dimensional electron – hole systems: Phase diagram and single-particle spectra, J. Phys. Soc. Japan **83**, 084702 (2014).

[31] F. Deschler, M. Price, S. Pathak, L. E. Klintberg, D. D. Jarausch, R. Higler, S. Hüttner, T. Leijtens, S. D. Stranks, H. J. Snaith, M. Atatüre, R. T. Phillips, and R. H. Friend, High photoluminescence efficiency and optically pumped lasing in solution-processed mixed halide perovskite semiconductors, J. Phys. Chem. Lett. **5**, 1421 (2014).

[32] P. Geiregat, J. Maes, K. Chen, E. Drijvers, J. De Roo, J. M. Hodgkiss, and Z. Hens, Using bulk-like nanocrystals to probe intrinsic optical gain characteristics of inorganic lead halide perovskites, ACS Nano **12**, 10178 (2018).

[33] S. W. Eaton, M. Lai, N. A. Gibson, A. B. Wong, L. Dou, J. Ma, L.-W. Wang, S. R. Leone, and P. Yang, Lasing in robust cesium lead halide perovskite nanowires, Proc. Natl Acad. Sci. U.S.A. **113**, 1993 (2016).

[34] T. Palmieri, E. Baldini, A. Steinhoff, A. Akrap, M. Kollár, E. Horváth, L. Forró, F. Jahnke, and M. Chergui, Mahan excitons in room-temperature methylammonium lead bromide perovskites, Nat. Commun. **11**, 1 (2020).

[35] Z. Wang, H. Sun, and C. Ning, Excitonic complexes and optical gain in two-dimensional molybdenum ditelluride well below the Mott transition, Light Sci. Appl. **9**, 39 (2020).

[36] G. Lifante, *Integrated Photonics: Fundamentals* (John Wiley & Sons, Chichester, West Sussex, 2002).

[37] E. Palik, *Handbook of Optical Constants of Solids* (Elsevier, San Diego, 1998).

[38] S. De Wolf, J. Holovsky, S. J. Moon, P. Löper, B. Niesen, M. Ledinsky, F. J. Haug, J. H. Yum, and C. Ballif, Organometallic halide perovskites: Sharp optical absorption edge and its relation to photovoltaic performance, J. Phys. Chem. Lett. **5**, 1035 (2014).

[39] L. M. Pazós-Outón, M. Szumilo, R. Lamboll, J. M. Ritcher, M. Crespo-Quesada, B. Ehrler, L. M. Pazos-Outon, M. Abdi-Jalebi, H. J. Beeson, M. Vrucinie, M. Alsari, H. J. Snaith, B. Ehrler, R. H. Friend, and F. Deschler, Organometallic halide perovskites: Sharp optical absorption edge and its relation to photovoltaic performance, Science. **351**, 1430 (2016).

[40] D. Hong, J. Li, S. Wan, I. G. Scheblykin, and Y. Tian, Redshifted photoluminescence from crystal edges due to carrier redistribution and reabsorption in lead triiodide perovskites, J. Phys. Chem. C **123**, 12521 (2019).

[41] C. Wehrenfennig, M. Liu, H. J. Snaith, M. B. Johnston, and L. M. Herz, Homogeneous emission line broadening in the organo lead halide perovskite $CH_3NH_3PbI_{3-x}Cl_x$, J. Phys. Chem. Lett. **5**, 1300 (2014).

[42] E. Rosencher and B. Vinter, *Optoelectronics* (Cambridge University Press, Cambridge, 2002).

[43] A. R. Goñi, A. Cantarero, K. Syassen, and M. Cardona, Effect of pressure on the low-temperature exciton absorption in GaAs, Phys. Rev. B **41**, 10111 (1990).

[44] J. Even, L. Pedesseau, and C. Katan, Analysis of multivalley and multibandgap absorption and enhancement of free carriers related to exciton screening in hybrid perovskites, J. Phys. Chem. C **118**, 11566 (2014).

[45] R. Chulia-Jordan, E. Mas-Marzá, A. Segura, J. Bisquert, and J. P. Martínez-Pastor, Crystalline-size dependence of dual emission peak on hybrid organic lead-iodide perovskite films at low temperatures, J. Phys. Chem. C **122**, 22717 (2018).

[46] J. Aguilar-Hernández, G. Contreras-Puente, H. Flores-Llamas, H. Yee-Madeira, and O. Zelaya-Angel, The temperature-dependence of the energy band gap of csvt-grown cdte films determined by photoluminescence, J. Phys. D. Appl. Phys. **28**, 1517 (1995).

[47] G. Brammertz, Y. Mols, S. Degroote, V. Motsnyi, M. Leys, G. Borghs, and M. Caymax, Low-temperature photoluminescence study of thin epitaxial GaAs films on Ge substrates, J. Appl. Phys. **99**, 093514 (2006).

[48] E. Grilli, M. Guzzi, R. Zamboni, and L. Pavesi, High-precision determination of the temperature dependence of the fundamental energy gap in gallium arsenide, Phys. Rev. B **45**, 1638 (1992).

[49] B. E. A. Saleh and M. C. Teich, *Fundamentals of Photonics* (John Wiley & Sons, New York, 1991).

[50] J. S. Manser and P. V. Kamat, Band filling with free charge carriers in organometal halide perovskites, Nat. Photonics **8**, 737 (2014).

[51] D. A. Valverde-Chávez, C. S. Ponseca, C. C. Stoumpos, A. Yartsev, M. G. Kanatzidis, V. Sundström, and D. G. Cooke, Intrinsic femtosecond charge generation dynamics in single crystal $CH_3NH_3PbI_3$, Energy Environ. Sci. **8**, 3700 (2015).

[52] M. J. Conelly, *Semiconductor Optical Amplifiers* (Cluwer Academic Publishers, New York, 2004).

[53] G. Giorgi, J. I. Fujisawa, H. Segawa, and K. Yamashita, Small photocarrier effective masses featuring ambipolar transport in methylammonium lead iodide perovskite: A density functional analysis, J. Phys. Chem. Lett. **4**, 4213 (2013).

[54] H. Zhang, Q. Liao, Y. Wu, Z. Zhang, Q. Gao, P. Liu, M. Li, J. Yao, and H. Fu, 2D ruddlesden–popper perovskites microring laser array, Adv. Mater. **30**, 1 (2018).

[55] M. Saliba, S. M. Wood, J. B. Patel, P. K. Nayak, J. Huang, J. A. Alexander-Webber, B. Wenger, S. D. Stranks, M. T. Hrantner, J. T. W. Wang, R. J. Nicholas, L. M. Herz, M. B. Johnston, S. M. Morris, H. J. Snaith, and M. K. Riede, Structured organic-inorganic perovskite toward a distributed feedback laser, Adv. Mater. **28**, 923 (2016).

[56] S. D. Stranks, S. M. Wood, K. Wojciechowski, F. Deschler, M. Saliba, H. Khandelwal, J. B. Patel, S. Elston, L. M. Herz, M. B. Johnston, A. P. H. J. Schenning, M. G. Debije, M. Riede, S. M. Morris, and H. J. Snaith, Enhanced amplified spontaneous emission in perovskites using a flexible cholesteric liquid crystal reflector, Nano Lett. **15**, 4935 (2015).

[57] H. Zhu, Y. Fu, F. Meng, X. Wu, Z. Gong, Q. Ding, M. V. Gustafsson, M. T. Trinh, S. Jin, and X.-Y. Zhu, Lead halide perovskite nanowire lasers with low lasing thresholds and high quality factors, Nat. Mater. **14**, 636 (2015).

[58] K. Wang, S. Sun, C. Zhang, W. Sun, Z. Gu, S. Xiao, and Q. Song, Whispering-gallery-mode based $CH_3NH_3PbBr_3$ perovskite microrod lasers with high quality factors, Mater. Chem. Front. **1**, 477 (2017).

[59] Q. Liao, K. Hu, H. Zhang, X. Wang, J. Yao, and H. Fu, Perovskite microdisk microlasers self-assembled from solution, Adv. Mater. **27**, 3405 (2015).

[60] S. Yakunin, L. Protesescu, F. Krieg, M. I. Bodnarchuk, G. Nedelcu, M. Humer, G. De Luca, M. Fiebig, W. Heiss, and M. V. Kovalenko, Low-threshold amplified spontaneous emission and lasing from colloidal nanocrystals of caesium lead halide perovskites, Nat. Commun. **6**, 8056 (2015).

[61] V. Gonzalez-pedro, E. J. Juarez-perez, W. Arsyad, E. M. Barea, F. Fabregat-santiago, I. Mora-sero, and J. Bisquert, General working principles of $CH_3NH_3PbX_3$ perovskite solar cells, Nano Lett. **14**, 888 (2013).

[62] H. Gordillo, I. Suarez, R. Abargues, P. Rodriguez-Canto, and J. P. Martinez-Pastor, Color tuning and white light by dispersing CdSe, CdTe, and CdS in PMMA nanocomposite waveguides, IEEE Photonics J. **5**, 2201412 (2013).

[63] L. W. Casperson and L. W. Casperson, Threshold characteristics of mirrorless lasers threshold characteristics of mirrorless lasers, J. Appl. Phys. **48**, 256 (1977).

[64] T. W. Crothers, R. L. Milot, J. B. Patel, E. S. Parrott, J. Schlipf, P. Müller-Buschbaum, M. B. Johnston, and L. M. Herz, Photon reabsorption masks intrinsic bimolecular charge-carrier recombination in $CH_3NH_3PbI_3$ perovskite, Nano Lett. **17**, 5782 (2017).

[65] See Supplemental Material at http://link.aps.org/supplemental/10.1103/PhysRevApplied.13.064071 for a complete list of symbols mentioned in the paper.